

 Very Important Paper


Olefin Ring-closing Metathesis under Spatial Confinement: Morphology–Transport Relationships

 Ulrich Tallarek,^{*,[a]} Janika Hochstrasser,^[a] Felix Ziegler,^[b] Xiaohui Huang,^[c] Christian Kübel,^[c, d] and Michael R. Buchmeiser^[b]

Spatial confinement effects on hindered transport in mesoporous silica particles are quantified using reconstructions of their morphology obtained by electron tomography as geometrical models in direct diffusion simulations for passive, finite-size tracers. We monitor accessible porosity and effective diffusion coefficients resulting from steric and hydrodynamic interactions between tracers and pore space confinement as a function of $\lambda = d_{\text{tracer}}/d_{\text{meso}}$, the ratio of tracer to mean mesopore size. For $\lambda = 0$, pointlike tracers reproduce the true diffusive tortuosities.

For $\lambda > 0$, derived hindrance factors quantify the extent to which diffusion through the materials is hindered compared with free diffusion in the bulk liquid. Morphology-transport relationships are then discussed with respect to the immobilization, formation, and transport of key molecular species in the ring-closing metathesis of an α,ω -diene to macro(mono)cyclization product and oligomer, with a 2nd-generation Hoveyda-Grubbs type catalyst immobilized inside the mesopores of the particles.

1. Introduction

The restricted access to and hindered diffusion within mesoporous materials are key transport phenomena of many technological and environmental processes. It includes the immobilization of bulky species (molecular catalysts, enzymes, polyhedra, and clusters) on the internal surface of a material,^[1] the transport of substrates to and products from the catalytically active sites,^[2] or the controlled release of drugs, macromolecules, and cells.^[3] For example, the partial size-exclusion of solutes from the mesopore space of a material during surface

functionalization diminishes its mass loadability and reduces the active surface area, and when the interfacial kinetics are fast, hindered diffusion to and from the active surface sites becomes limiting to the process performance.^[4] Therefore, the impact of restricted access and hindered diffusion, the result of steric and hydrodynamic interactions between solutes and the confinement, should be quantitatively known to unravel the complex interrelationships between morphology, transport, and reaction and thereby allow for a better tuning of efficiency, yield, and selectivity. This is particularly important for multifunctional catalysts designed to achieve higher catalytic activity or enantioselectivity, because transport under confinement triggers synergistic effects between different functionalities immobilized on the same surface.^[5]

Hindrance to diffusion of passive, finite-size tracer molecules (or solutes) within and through a mesopore network is commonly expressed by the local and global hindrance factors $K_d(\lambda)$ and $H(\lambda)$ as a function of $\lambda = d_{\text{tracer}}/d_{\text{meso}}$, the ratio of the hydrodynamic diameter of the tracers (d_{tracer}) and the mean mesopore diameter (d_{meso}).^[6]

$$H(\lambda) = \frac{D_{\text{eff,H}}(\lambda)}{D_m} = K_d(\lambda)\varepsilon(\lambda) \quad (1)$$

The effective diffusion coefficient $D_{\text{eff,H}}(\lambda)$ in Eq. (1) characterizes the global process of diffusion into and through the mesopore network (subscript H) and $H(\lambda)$ is the global hindrance factor relating $D_{\text{eff,H}}(\lambda)$ to D_m , the diffusion coefficient for free diffusion in the bulk liquid. In contrast, $K_d(\lambda) = D_{\text{eff,K}}(\lambda)/D_m$ denotes the local hindrance factor representing effective diffusion locally within the mesopore network (subscript K). $\varepsilon(\lambda)$ in Eq. (1) characterizes the accessible mesoporosity as a function of λ . Accordingly, $D_{\text{eff,K}}(\lambda) = D_{\text{eff,H}}(\lambda)/\varepsilon(\lambda)$.


Hindered diffusion behaviour expressed by Eq. (1) and the underlying morphology-transport relationships can be elucidated by a combination of experimental approaches.^[7] For


[a] Prof. U. Tallarek, J. Hochstrasser
 Department of Chemistry
 Philipps-Universität Marburg
 Hans-Meerwein-Strasse 4
 D-35032 Marburg (Germany)
 E-mail: tallarek@staff.uni-marburg.de


[b] F. Ziegler, Prof. M. R. Buchmeiser
 Institute of Polymer Chemistry
 Universität Stuttgart
 Pfaffenwaldring 55
 D-70569 Stuttgart (Germany)

[c] X. Huang, Prof. C. Kübel
 Institute of Nanotechnology and Karlsruhe Nano Micro Facility
 Karlsruhe Institute of Technology (KIT)
 Hermann-von-Helmholtz-Platz 1
 D-76344 Eggenstein-Leopoldshafen (Germany)

[d] Prof. C. Kübel
 Department of Materials and Earth Sciences
 Technische Universität Darmstadt
 Alarich-Weiss-Strasse 2
 D-64287 Darmstadt (Germany)

 Supporting information for this article is available on the WWW under <https://doi.org/10.1002/cctc.202001495>

 This publication is part of a Special Collection on "Catalysis in Confined Spaces". Please check the ChemCatChem homepage for more articles in the collection.

 © 2020 The Authors. ChemCatChem published by Wiley-VCH GmbH. This is an open access article under the terms of the Creative Commons Attribution License, which permits use, distribution and reproduction in any medium, provided the original work is properly cited.

example, pulsed field-gradient nuclear magnetic resonance (PFG-NMR) has been widely applied to study effective diffusion coefficients in mesoporous materials used in heterogeneous catalysis.^[8] The ensemble-tracking offered by PFG-NMR can be complemented by single-molecule tracking data from spectroscopic techniques that allow to monitor trajectories of single molecules and localize their position of sorption and reaction,^[9] or even track diffusion in a pore while imaging the pore itself and thus quantify diffusion at the single-pore level.^[10] IR microimaging, on the other hand, has been implemented to determine effectiveness factors of catalyst particles in a single measurement by recording the evolution of substrate and product concentration profiles emerging from the direct interplay of diffusion and reaction.^[11]

However, utilizing spatial confinement effects in the best possible way implies that the three-dimensional morphology of the mesopore space under consideration is known, for example, by reconstruction via electron tomography^[12] (becoming increasingly popular as part of multiscale characterization studies^[13]), and transferred into geometrical models that are subsequently used in direct, i.e., pore-scale simulations of diffusion, sorption, and reaction. This approach provides a comprehensive picture regarding the spatiotemporal dynamics of relevant physicochemical phenomena under explicit consideration of the three-dimensional morphology of a material, reflecting its individual preparation history. Further, diffusion can be simulated independently from processes coupled in experiments, such as sorption and reaction, by using passive tracers that neither interact with the material surface nor with one another. It allows to quantitatively resolve key aspects of diffusive transport in porous media, such as the effect of increasing tracer size on hindrance to diffusion. In addition, transport properties can be related to morphological characteristics, for example, to the porosity and connectivity of the accessible pore space, which leads in a straightforward manner to the morphology-transport relationships reflected by the local hindrance factor $K_d(\lambda)$ and the accessible porosity function $\varepsilon(\lambda)$ in Eq. (1).

We recently presented a three-step methodology comprising (i) the physical reconstruction of the mesopore space by electron tomography, (ii) morphological analysis of the reconstructed mesopore space regarding, for example, its pore network connectivity and the presence of dead ends, constrictions, and closed pores, and (iii) direct numerical simulation of tracer diffusion in the reconstructed mesopore space with systematic variation of the fundamental parameter λ to derive expressions for the hindrance to diffusion in ordered and random mesoporous silicas.^[14] These studies provided two main conclusions. First, expressions for hindered diffusion decrease more strongly with increasing λ than predicted by the equations of Renkin^[15] and Dechadilok and Deen.^[6b] Those equations were derived for diffusion of spherical particles in a cylindrical pore by resolving the problem of enhanced drag from the hydrodynamic Stokes-friction effect. It appears unsurprising that three-dimensional networks of pores with varying shape, size, and connectivity close off at lower λ due to bottlenecks at smaller pore openings than a single, straight

cylinder. Morphology-transport relationships of a material are its signature, reflecting individual morphological features as the consequence of its often highly specific preparation history.^[14c] Second, ordered mesoporous silicas enable more selective access to the mesopore space (closing off sharper with larger tracer size) than random mesoporous silicas.^[14d] From that perspective the main benefit of the studied ordered silicas (SBA-15 and KIT-6) is a narrow pore size distribution that, in turn, increases the size-selectivity of a process. On the other hand, ordered silicas did not provide faster diffusion than the random silicas. Morphological analysis has shown that diffusion in a pore space with a narrow pore size distribution becomes highly sensitive to local nonuniformities in pore shape, size, and connectivity. Thus, hindered diffusion observed on a macroscopic scale depends critically on local aspects of pore interconnectivity and the actual deviations from idealized pore geometries. This sensitivity to details of the pore space suggests that structural properties as manifested in XRD patterns and a narrow pore size distribution are unreliable predictors of the transport dynamics and that quantitative measures of morphological and transport properties require physical reconstruction of the mesoporous materials.^[14d]

Motivated by these results, we initiated further research on potential benefits of ordered vs. random pore structures and narrow vs. wide pore size distributions for the transport properties of mesoporous silica materials employed as support structures in heterogeneous catalysis. An additional goal was to establish a continuous-flow microreactor platform to complement the insight coming from simulations and for comparison with batch experiments. In this work, we present our first results on the morphology-transport-functionality relationships for spherical silica particles with a mean particle size of $\sim 5 \mu\text{m}$ and mean nominal mesopore sizes of 6 and 10 nm employed in the ring-closing metathesis (RCM) of an α,ω -diene with a 2nd-generation Hoveyda-Grubbs type catalyst selectively immobilized inside their mesopores. While catalyst immobilization generally aims at improved catalyst stability, its separation from the reaction mixture, and reuse of the catalyst, and many approaches are available today for immobilization of Grubbs-type catalysts on organic and inorganic supports,^[16] another highly attractive feature of catalyst immobilization in mesopores of different size and shape is the confinement effect and its impact on catalyst selectivity.^[5,17] This has been highlighted with a biomimetic approach that employs a biological concept to reduce the drawbacks related to macrocyclization.^[18] The concept is based on pore size-selective immobilization of a ruthenium-based olefin metathesis catalyst inside the pores of a support. If the pore diameter is tuned such that only one substrate molecule can approach the catalyst inside a pore at a given time, then macro(mono)cyclization (MMC) will prevail and oligomerization (O) should be suppressed. With this approach, the ratio between MMC product and all undesired O products resulting from acyclic diene metathesis polymerization (ADMET) could be increased from 0.55, corresponding to 35% MMC product obtained with the homogeneous catalyst, up to 1.49, corresponding to 60% MMC product.^[18] Importantly, a relation-

ship between the MMC/O ratio and the substrate-to-pore-size ratio has been established in that work.

Here, we build on our accumulated experience with the reconstruction-simulation approach as applied to mesoporous silicas^[14] and the experimental results achieved with the biomimetic approach to fine-tune spatial confinement effects for increased macrocyclization selectivity.^[18] We start with illustrating the individual steps necessary to establish morphology-transport relationships for the silica particles, which – due to their different pore size distributions and mean mesopore sizes at conserved particle size – reveal different solute-size selective transport properties. Confinement effects on hindered transport are quantified by using the reconstructed pore space morphologies as geometrical models in diffusion simulations with finite-size tracer molecules. Accessible porosity and effective diffusion coefficients are recorded systematically as a function of λ , the ratio between the hydrodynamic diameter of the tracers and the mean mesopore diameter. These relationships, general functions of λ for the investigated materials, are then specifically discussed in view of the transport properties of the homogeneous catalyst (relevant for its immobilization inside the mesopores), substrate molecules (relevant for catalyst accessibility in the pores), as well as the MMC and O products (relevant for their formation via competitive olefin metathesis pathways).

2. Results and Discussion

2.1. Properties of the bulk mesoporous silica samples

Structural properties of the silica particles with nominal mesopore diameters of 60 and 100 Å (the two materials are accordingly denoted as Si60 and Si100 further on) obtained by nitrogen physisorption measurements are summarized in Table 1.

The nitrogen physisorption isotherms of the mesoporous silicas in Figure 1A can be assigned to type IV(a) isotherms with H2(a) hysteresis loops.^[19] Derived pore size distributions in Figure 1B have relative standard deviations of 59% (Si60) and 38% (Si100). These are typical values for random mesoporous silicas used, for example, in liquid chromatography, where pore size distributions with relative standard deviations of 30–50% and higher are found, often with a tail towards larger pore sizes.^[14b,c,20] The mean pore size is 5.9 nm for Si60 and 13.0 nm for Si100 (corresponding here to the mode of each distribution). These values were subsequently used to calculate $\lambda = d_{\text{tracer}}/d_{\text{meso}}$. Cumulative pore volumes shown in Figure 1C confirm the existence of micropores in Si60 (see inset). However, the amount of micropores is negligible compared to the main pore volume starting with pores of diameters above 2 nm. For Si100, the smallest pore size is 6 nm. Finally, the intraparticle porosities ϵ_{intra} (intraparticle void volume fractions) are 63% and 72% for Si60 and Si100, respectively. The higher porosity of the Si100 material can be rationalized with its preparation history based on a pore widening of small-pore silica (hydrothermal treatment), which also leaches some of the solid, resulting in wider pores and a somewhat higher porosity.

Parameter ^[a]	Si60	Si100
V_t [cm ³ g ⁻¹]	0.82	1.19
S_{BET} [m ² g ⁻¹]	793	417
d_{meso} [nm]	5.9	13.0
ϵ_{intra} [–]	0.63	0.72

[a] Total pore volume (V_t), specific surface area (S_{BET}), and mode mesopore diameter (d_{meso}) derived from nitrogen physisorption analysis; intraparticle porosity (ϵ_{intra}) calculated by $\epsilon_{\text{intra}} = V_t / (V_t + \delta_{\text{Si}}^{-1})$, where δ_{Si} is the density of amorphous silica (2.13 g cm⁻³).

2.2. Three-dimensional reconstruction of mesopore space morphologies

For statistical reasons, four reconstructions were prepared in total from each silica material using electron tomography. Two of the reconstructions are shown in Figure 2, and the complete set of the (eight) reconstructions as well as their dimensions are summarized in the Supporting Information (Figure S1 and

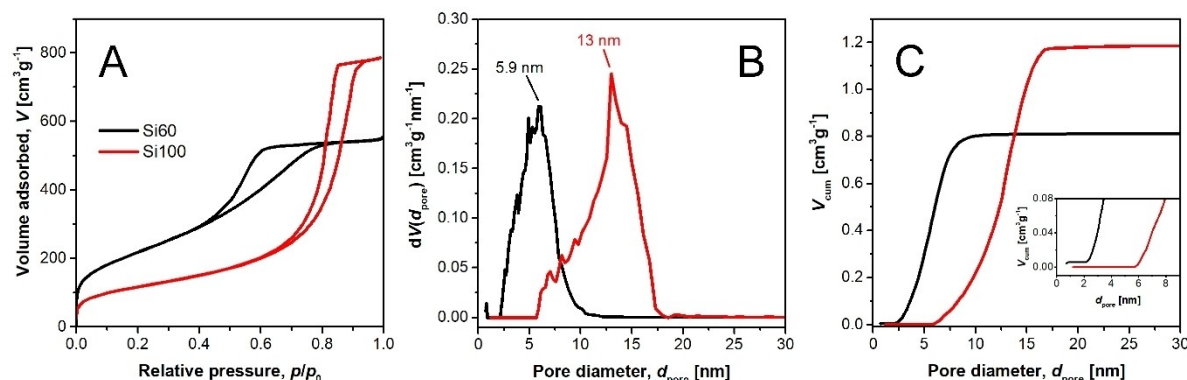


Figure 1. Nitrogen physisorption isotherms (A), pore size distributions (B), and cumulative pore volumes (C) for the two silica powder samples.

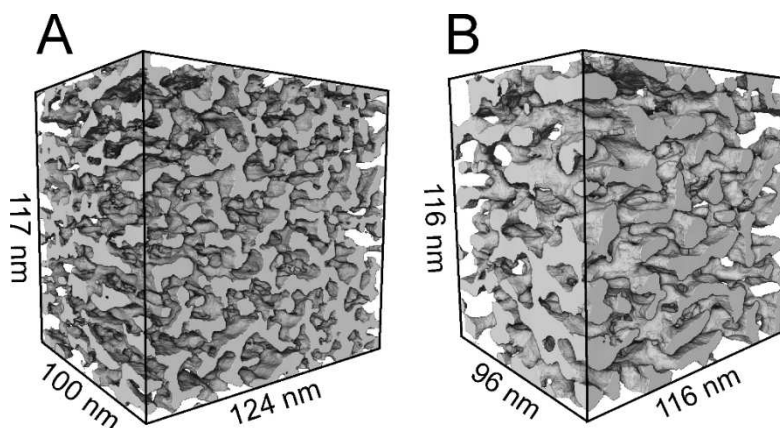


Figure 2. Selected reconstructions of the Si60 (A) and Si100 (B) mesoporous silicas (see Figure S1, Supporting Information, for the complete set of reconstructions).

Table S1). Reconstructions highlighted in Figure 2 and Figure S1 clearly visualize the different geometrical properties of Si60 and Si100 materials with respect to their mean pore size. Average void volume fractions, i.e., the fractions of void voxels in the two sets of reconstructions, are 60.1% for Si60 and 69.1% for Si100, values that are very similar to the porosities based on nitrogen physisorption analysis (ϵ_{intra} in Table 1). The reconstructions slightly underestimate the nitrogen sorption data (by $\sim 4\%$), possibly due to some smaller pores or pore necks that escape proper identification as void during the reconstruction procedure. For both silicas, we observe a highly interconnected, random mesopore network confined by solid (impenetrable) silica walls.

2.3. Morphology-transport relationships: Accessible porosity and hindered diffusion

Direct (pore-scale) simulations of hindered diffusion are conducted for pointlike and finite-size tracers that move through the pore space of the reconstructions driven by random

Brownian motion. The pore space accessible to an ensemble of pointlike tracers equals the entire void volume of a reconstruction. However, due to their steric interactions with the pore walls, finite-size tracers have access to only parts of that volume, depending on $\lambda = d_{\text{tracer}}/d_{\text{meso}}$, the ratio of the hydrodynamic diameter of the tracers (d_{tracer}) and the mean mesopore diameter (d_{meso}). To model the accessible porosity for finite-size tracers, the reconstructions (serving as geometrical models in the simulations) are subjected to a dilation procedure illustrated by Figure 3.^[14,21] The reduction of accessible pore space for finite-size tracers can be accounted for by eroding the pore space accessible to pointlike tracers with a structuring element of size d_{tracer} . Accordingly, a layer of solid is added to the silica walls (Figure 3A and 3B), where the layer-thickness equals half the diameter of the finite-size tracer (Figure 3C). By this procedure, the steric interaction between the center (point) of the finite-size tracer and the hard silica wall is modelled, i.e., the center of a hard spherical tracer particle of diameter d_{tracer} is excluded from a region of thickness $d_{\text{tracer}}/2$ at the wall. The remaining porosity corresponds to the volume accessible to a tracer of size d_{tracer} . In other words, the void space accessible to

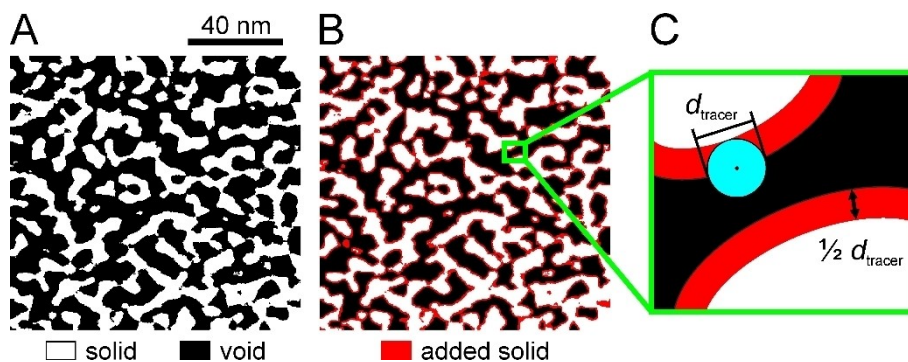


Figure 3. Schematic illustration of the dilation procedure. Solid phase (white) in the binary image stack (A) is dilated by a layer of additional solid (red) with thickness $\frac{1}{2} d_{\text{tracer}}$ (B). This represents the region adjacent to the pore walls, from which the center of a spherical, finite-size tracer of size d_{tracer} is excluded (C). The situation is equivalent to using pointlike tracers in the remaining (black) pore space.

the center of a finite-size tracer becomes identical to the void space accessible to a pointlike tracer if the pore size reduced by d_{tracer} .

The void volume fractions (accessible porosities) resulting for finite-size tracers of different diameter d_{tracer} are shown in Figure 4A for both sets of reconstructed silicas. Error bars represent 95% confidence intervals for the four reconstructions of each set. Pointlike tracers ($d_{\text{tracer}}=0$) experience an average porosity of $\varepsilon_0=0.601$ in Si60 and $\varepsilon_0=0.691$ in Si100. These values are (expectedly) identical to the average porosities calculated from the fractions of void voxels in the four reconstructions for each silica. It confirms that the pointlike tracers have access to every voxel in a reconstruction. Due to the smaller mean pore size the accessible porosity declines faster with increasing d_{tracer} for Si60 than for Si100 (Figure 4A). Effective diffusion coefficients simulated for finite-size tracers in the available pore spaces are shown in Figure 4B (normalized by D_0 , the diffusion coefficients for pointlike tracers in the reconstructions). As expected, the mobility of larger tracers is reduced compared to pointlike tracers and decreases more quickly for Si60 than for Si100. In both materials, diffusion is hindered by the intrinsic confinement including the tortuosity and constrictivity of the pores.

Figure 5 (top row) highlights pore constrictions in both materials (red circles), which become closed, i.e., inaccessible pathways for larger tracers (bottom row) due to their enhanced steric interaction with the pore walls. Also the zoomed regions (green frames) highlight the substantial decrease of accessible porosity and the expected increased hindrance to diffusion for different tracer sizes (top row: pointlike tracers, bottom row: $d_{\text{tracer}}=1.4$ nm and 1.9 nm), as illustrated here by the dilation procedure. Finally, the green cylinders in Figure 5 with the respective mean diameter d_{meso} (from each silica) indicate consistency between the physisorption-based analysis and pore sizes found in the physical reconstructions.

To quantify the hindrance to diffusion in both silicas in a dimensionless form, the accessible porosity, normalized by $\varepsilon_0 \equiv \varepsilon(\lambda=0)$, and the simulated effective diffusion coefficient, normalized by $D_0 \equiv D_{\text{eff},K}(\lambda=0)$, were plotted as a function of $\lambda = d_{\text{tracer}}/d_{\text{meso}}$, the ratio between tracer size and mean mesopore diameter. The resulting data sets are summarized in Figure 6 and the following second-order polynomial fits are obtained for the porosity (Figure 6A):

$$\frac{\varepsilon(\lambda)}{\varepsilon_0} = 1 - 2.02\lambda + 0.86\lambda^2 \quad (\text{Si60}) \quad (2)$$

$$\frac{\varepsilon(\lambda)}{\varepsilon_0} = 1 - 2.56\lambda + 1.49\lambda^2 \quad (\text{Si100}) \quad (3)$$

For the effective diffusion coefficients, we receive the following third-order polynomial fits (Figure 6B):

$$\frac{D_{\text{eff},K}(\lambda)}{D_0} = 1 - 1.09\lambda - 2.54\lambda^2 + 3.17\lambda^3 \quad (\text{Si60}) \quad (4)$$

$$\frac{D_{\text{eff},K}(\lambda)}{D_0} = 1 - 0.89\lambda - 5.64\lambda^2 + 7.42\lambda^3 \quad (\text{Si100}) \quad (5)$$

With Eqs. (2)–(5) we can construct the global hindrance factor $H(\lambda)$ for the two materials (cf. Eq. (1)). Because $K_d(\lambda) = D_{\text{eff},K}(\lambda)/D_m = D_{\text{eff},K}(\lambda)/D_0\tau_0$ (where τ_0 denotes the diffusive tortuosity of the pointlike tracers), we obtain for Si60:

$$H(\lambda) = K_d(\lambda)\varepsilon(\lambda) = \frac{\varepsilon_0}{\tau_0}(1 - 3.11\lambda + 0.52\lambda^2 + 7.36\lambda^3 - 8.58\lambda^4 + 2.73\lambda^5) \quad (6)$$

And for Si100 we receive:

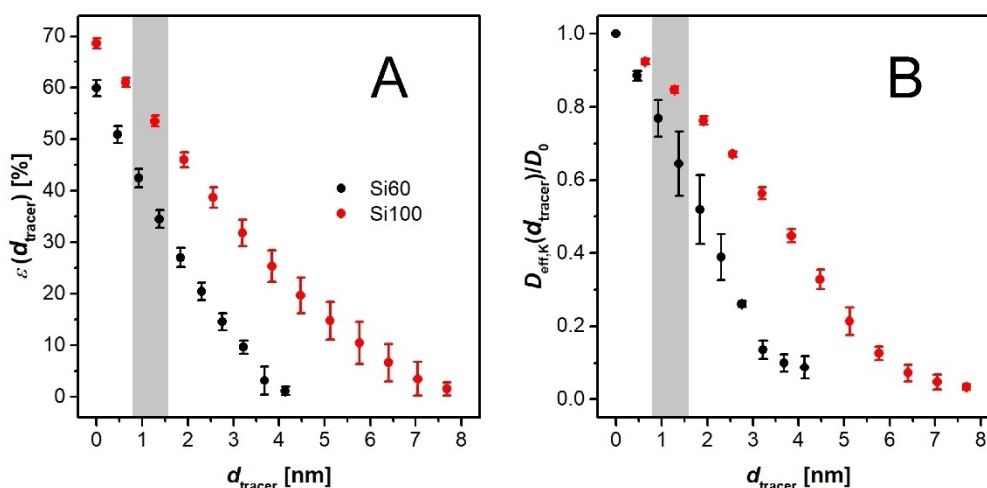


Figure 4. Accessible porosity (A) and simulated effective diffusion coefficient (B) as a function of tracer size d_{tracer} for Si60 and Si100. Diffusion coefficients are normalized by $D_0 \equiv D_{\text{eff},K}(d_{\text{tracer}}=0)$, the diffusion coefficient obtained in the limiting case of $d_{\text{tracer}}=0$. The gray-shaded regions will become relevant to the discussion in Section 2.4.

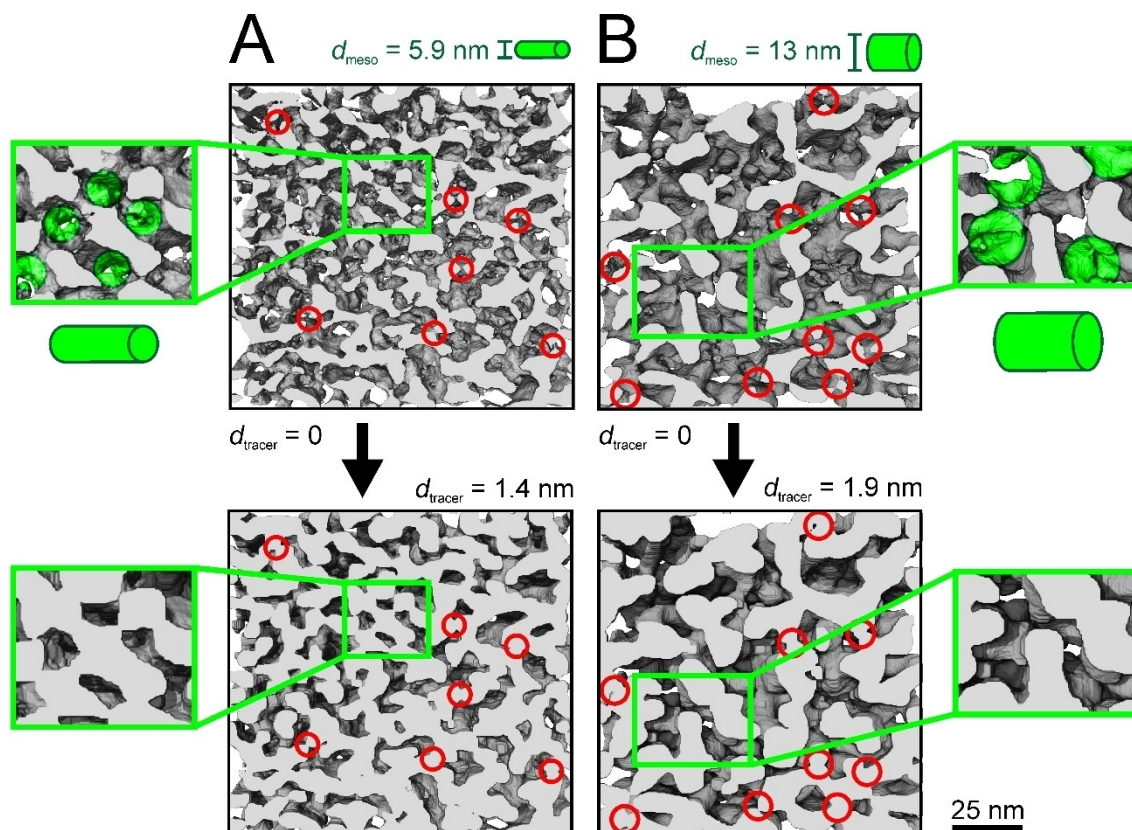


Figure 5. (Top row) Front view on two original reconstructions of Si60 (A) and Si100 (B) and after application of the dilation procedure (bottom row). Red circles highlight constrictions that are open for pointlike tracers (top row, $d_{\text{tracer}} = 0$), but closed for finite-size tracers (bottom row, $d_{\text{tracer}} = 1.4$ nm and 1.9 nm).

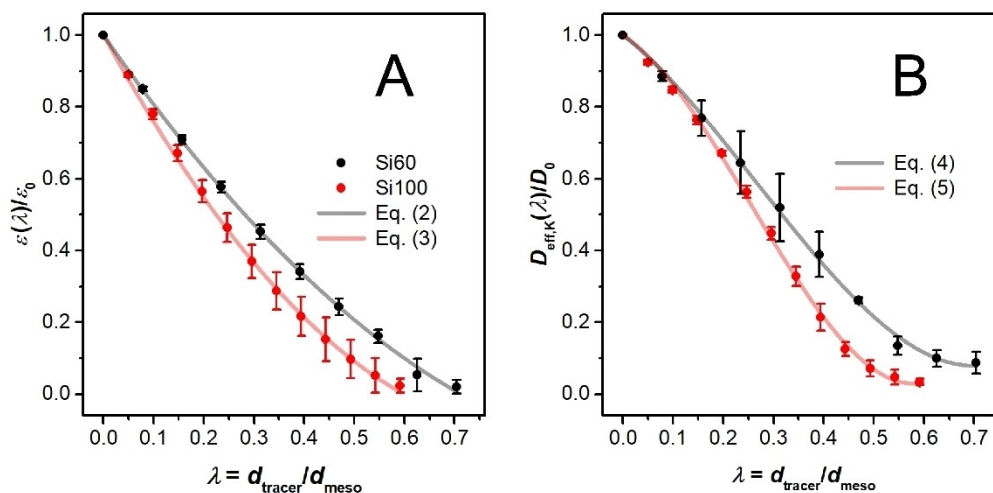


Figure 6. Dependence of the accessible porosity (A) and effective diffusive mobility (B) in physical reconstructions of the two mesoporous silicas on λ , the ratio of tracer size to mean mesopore diameter. Data are normalized by the corresponding values for pointlike tracers, $\epsilon_0 \equiv \epsilon(\lambda = 0)$ and $D_0 \equiv D_{\text{eff},K}(\lambda = 0) = D_m/\tau_0$ (with τ_0 , the diffusive tortuosity of the pointlike tracers).

$$H(\lambda) = K_d(\lambda)\epsilon(\lambda) = \frac{\epsilon_0}{\tau_0} (1 - 3.45\lambda - 1.87\lambda^2 + 20.5\lambda^3 - 27.4\lambda^4 + 11.1\lambda^5) \quad (7)$$

Inserting the respective values of ϵ_0 and τ_0 , i.e., accessible porosity and diffusive tortuosity for pointlike tracers ($\epsilon_0 = 0.601$ and $\tau_0 = 1.69$ for Si60, $\epsilon_0 = 0.691$ and $\tau_0 = 1.41$ for Si100) into Eqs. (6) and (7) allows to quantify hindered diffusion of finite-size, passive tracers into and through both silicas for any λ -

value. With the panels in Figure 6, the global hindrance factor $H(\lambda) = D_{\text{eff,H}}(\lambda)/D_m$ is obtained by multiplying the $\varepsilon(\lambda)/\varepsilon_0$ -value at a λ of interest in Figure 6A with the corresponding value for $D_{\text{eff,K}}(\lambda)/D_0$ in Figure 6B, the result of which represents the value given by the bracket expression in Eq. (6) or Eq. (7), and then multiplying the value with ε_0/τ_0 for a particular material.

2.4. Implications for molecular transport and selectivity in olefin metathesis

With the available relationships between pore space accessibility, effective diffusion, and tracer size for the two mesoporous silicas, Eqs. (2)–(7), we can now discuss consequences for the immobilization, formation, and transport of the key molecules 1–4 shown in Figure 7. Using hydrodynamic diameters d_H in bulk solution determined via DOSY-NMR measurements (see Experimental Section), we first identify corresponding values of $\lambda = d_H/d_{\text{meso}}$ and then calculate accessible porosity $\varepsilon(\lambda)$ as well as the local and global hindrance factors $K_d(\lambda)$ and $H(\lambda)$ for all species 1–4. These data are summarized in Table 2 for Si60 and Si100.

We begin our discussion with the immobilization of the catalyst 1 inside the mesopores of the silica particles, where the trimethoxysilyl tether (Figure 7) serves for covalent bonding to the surface silanol groups. Importantly, already this first step (catalyst immobilization) is a pore size-selective process. Caused

by a hydrodynamic diameter of $d_H = 1.08$ nm in benzene (solvent used for immobilization), the catalyst may be actually size-excluded from a significant number of pores. In Si60, 1 experiences an effective porosity of $\varepsilon(\lambda) = 0.395$. This corresponds to only ~66% of the porosity seen by the pointlike tracers ($\varepsilon_0 = 0.601$). In contrast, the porosity of the catalyst in Si100 (0.554) still represents 80% of the void space accessible to pointlike tracers ($\varepsilon_0 = 0.691$). Therefore, we predict a significantly lower loading with 1 for the Si60 than for the Si100 particles. In addition, diffusion of 1 into and through the pore space of Si60 is only half as fast as for Si100, as shown by the $H(\lambda)$ -values in Table 2. For example, the $H(\lambda)$ of 0.172 for Si60 means that the effective diffusion coefficient of 1, characterizing its global process of diffusion into (entering) and through (translocation) the mesopores, is only $0.172 \times D_m$ (cf. Eq. (1)), where D_m denotes the free diffusion coefficient of 1 in the bulk solution. This implies that correspondingly more time should be reserved in protocols for catalyst immobilization in Si60 than in Si100. In general, these times should also consider (together with the diffusive hindrance factors) the actual size of the particles that shall be uniformly modified to accurately fine-tune the overall immobilization step.

While the partial size-exclusion of the catalyst from the mesopore space of the silica particles during immobilization reduces their loadability and thus their active surface area, it should not affect the availability of immobilized catalyst by substrate 2 during the RCM experiments (in absolute toluene as

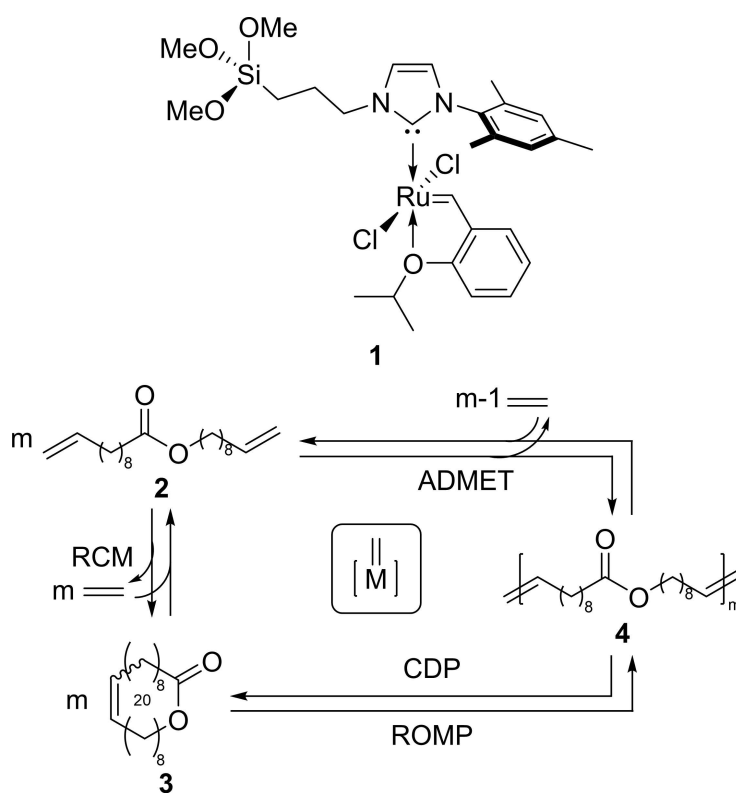


Figure 7. 2nd-generation Hoveyda-Grubbs type catalyst 1 immobilized inside the mesopores of the silica particles and olefin metathesis pathways for the α,ω -vinyl lactone 2 (substrate) to MMC product 3 and oligomer 4. RCM: ring-closing metathesis, ADMET: acyclic diene metathesis, ROMP: ring-opening metathesis polymerization, CDP: cyclodepolymerization.

Table 2. Transport properties of catalyst **1**, substrate **2**, macro(mono)cyclization product **3**, and oligomer **4** (cf. Figure 7) in bulk solution and in the mesoporous silicas.

Material	Parameter ^[a]	1	2	3	4
Si60	d_{H} [nm]	1.08	1.01	0.87	1.49
	$\lambda = d_{\text{H}}/d_{\text{meso}}$	0.18	0.17	0.15	0.25
	$\varepsilon(\lambda)$	0.395	0.407	0.432	0.327
	$K_{\text{d}}(\lambda)$	0.435	0.447	0.470	0.364
	$H(\lambda)$	0.172	0.182	0.203	0.119
Si100	d_{H} [nm]	1.08	1.01	0.87	1.49
	$\lambda = d_{\text{H}}/d_{\text{meso}}$	0.083	0.078	0.067	0.115
	$\varepsilon(\lambda)$	0.554	0.562	0.579	0.505
	$K_{\text{d}}(\lambda)$	0.628	0.634	0.646	0.590
	$H(\lambda)$	0.348	0.357	0.374	0.298

[a] Hydrodynamic diameter d_{H} in bulk solution (deuterated benzene for **1**, deuterated toluene for **2–4**) from DOSY-NMR diffusion measurements using the Stokes-Einstein equation; accessible porosity $\varepsilon(\lambda)$, local and global hindrance factors $K_{\text{d}}(\lambda)$ and $H(\lambda)$ calculated by Eqs. (2), (3), (6), and (7) with $\varepsilon_0 = 0.601$ and $\tau_0 = 1.69$ for Si60 and $\varepsilon_0 = 0.691$ and $\tau_0 = 1.41$ for Si100.

solvent). As seen in Table 2, the substrate is slightly smaller than the catalyst (1.01 vs. 1.08 nm) and should therefore experience no difficulties to reach all catalyst groups that could be immobilized on a silica surface. This is confirmed by the very similar accessible porosities $\varepsilon(\lambda)$ for **1** and **2** in the two silicas (Table 2). Also for the targeted MMC product **3**, still smaller than the substrate (0.87 vs. 1.01 nm), moving away from the catalyst (where it is formed) and out of the particles should be unproblematic. The situation changes, however, for the oligomer **4** that forms by ADMET in sufficiently large pores.^[18] Due to steric reasons, **4** in Figure 7 (and Table 2) mostly represents the dimer. With $d_{\text{H}} = 1.49$ nm, **4** is $\sim 70\%$ larger than **3** and has, with $\varepsilon(\lambda) = 0.327$ in Si60 (0.505 in Si100), access to only $\sim 76\%$ (87%) of the pore space seen by the MMC product **3**. Expectedly, also local diffusion of **4** within the mesopores (reflected by the $K_{\text{d}}(\lambda)$ -values in Table 2) is slower than for **3** and, as with the accessible porosity, the mobility difference increases with the increasing confinement (decreasing d_{meso}) from Si100 to Si60: For Si100 (Si60), the local hindrance factor of **4** is 0.590 (0.364) and has thus dropped to $\sim 91\%$ ($\sim 77\%$) of the corresponding value for **3**.

The enhanced confinement effect on the accessible porosity and effective diffusivity can be clearly recognized in Figure 4. The gray-shaded region in each panel indicates the range of hydrodynamic diameters d_{H} of the key molecular species (cf. Figure 7 and Table 2) involved in the RCM of interest. Importantly, porosity and diffusivity data for Si60 in Figure 4 are not just below those for Si100, but also their slopes are steeper. That is, the sensitivity of the increased spatial confinement to the size of the diffusing tracers is enhanced, as confirmed by the data in Table 2. On the other hand, it should be realized that the better size-selectivity of Si60 comes at the price of a reduced mobility (adversely affecting conversion). For example, the $H(\lambda)$ -value characterizing diffusion of substrate **2** into and through Si60 (0.182) has dropped to almost 50% of the value for Si100 (0.357). As a consequence, adequate supply of **2** may not be maintained. Depending on particle size and catalyst reactivity, this can severely increase the risk of diffusion limitations.^[4]

Figure 8 illustrates the important effect of accessible/excluded pore volumes associated with increasing tracer size (data based on Figure 4A for Si60). The representations, obtained for pairs of neighbored d_{tracer} -values (cf. Figure 4A), highlight pore volumes that become inaccessible when the tracer size is increased from $d_{\text{tracer},1}$ to $d_{\text{tracer},2}$. The top row visualizes accessible pore networks for a two-dimensional slice through Si60 (green and red: accessible to $d_{\text{tracer},1}$, green: accessible to $d_{\text{tracer},2}$), while the bottom row extracts three-dimensional pore volumes that are inaccessible to tracers of size $d_{\text{tracer},2}$ (in each panel). Interestingly, tracer sizes in Figure 8C represent (approximately) the hydrodynamic diameters of substrate **2** and product **4**, so that the excluded pore volume visualized in the bottom panel of Figure 8C identifies pores, in which **2** selectively reacts to the MMC product **3** via direct RCM. Due to its size, **4** can neither be formed in these pores nor enter (and diffuse through) them. Figure 8 therefore reveals that the diffusion networks for **2** and **3** are rather similar, but still significantly different (regarding pore volume, network connectivity, and tortuosity) from the transport pathways of **4**.

A conclusion from the previous analysis is that it should be possible to locally trap oligomer **4** in pore environments, which enable catalyst **1** and substrate **2** to enter but prevent the larger oligomer molecules from leaving. The existence of such regions is confirmed with Figure 9, which highlights (light blue) two examples of pore space in Si60 that can only be entered and left through constrictions (black circles). As indicated in the figure, these constrictions are wide enough for **1** (during immobilization) and **2** (during RCM) but too narrow for **4**. Consequently, it is possible that oligomer forms locally due to ADMET and then becomes sterically trapped. On the other hand, this occasional event does not comprise a dead end in the synthetic pathway of **4**. Because of equilibrium RCM, which can convert the oligomer into MMC product through cyclo-depolymerization (Figure 7),^[22] and the reversibility of ADMET (particularly in a compact microreactor without efficient loss of ethylene as the olefinic coproduct), organic matter stored locally in the oligomer may not be trapped forever, but can be released via further reactions of **4** resulting in sufficiently small molecules. The dynamics of the coupled reactions highlighted

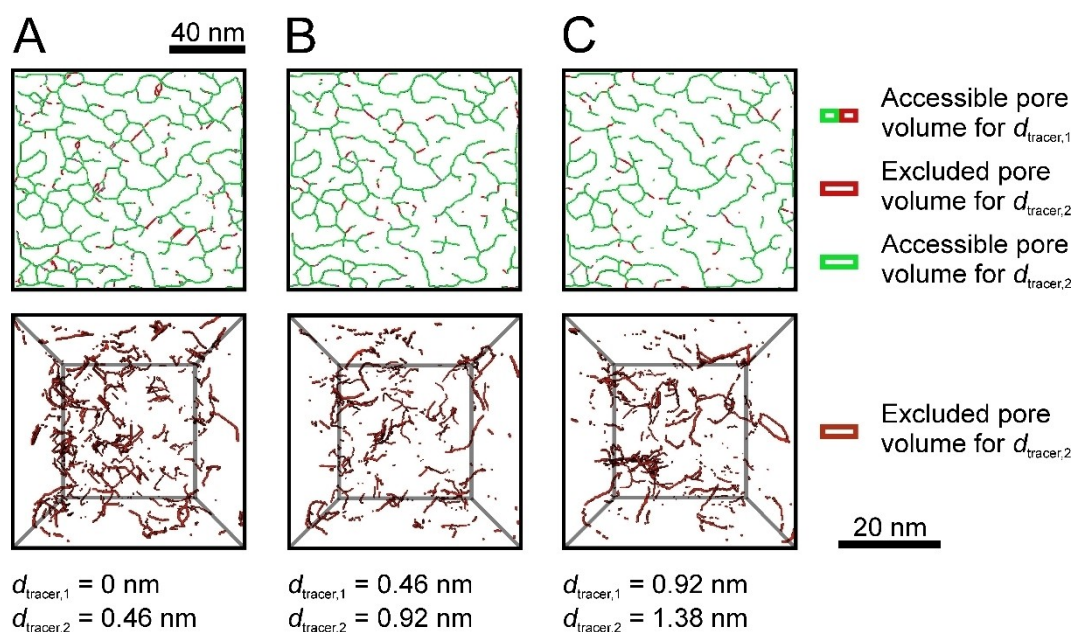


Figure 8. Accessibility of pores in Si60 to tracers of different size. Red pores indicate regions that become inaccessible when steric interaction between tracers and solid silica increases from $d_{\text{tracer},1}$ to $d_{\text{tracer},2}$. The top row highlights accessible pores for $d_{\text{tracer},1}$ and $d_{\text{tracer},2}$ in a single slice through the reconstruction, while the bottom row visualizes the size-exclusion volumes in cubic boxes with dimensions of 46^3 nm^3 .

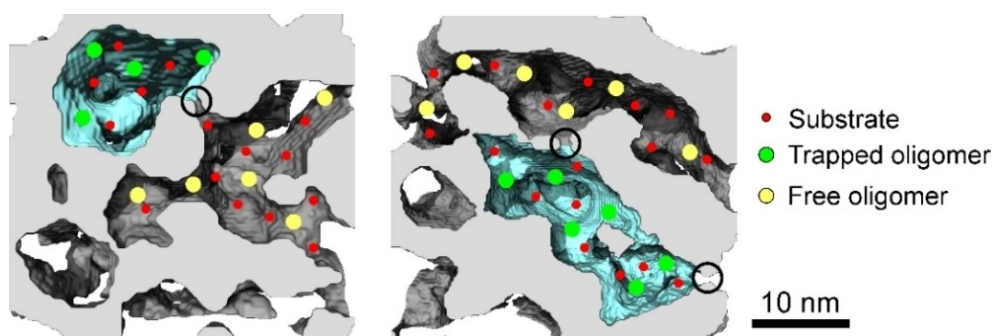


Figure 9. Local trapping of oligomer 4 in Si60. Highlighted in light blue are pore regions from which oligomer (formed locally within these regions) cannot escape by diffusion, because pore necks (black circles) are too narrow. On the other hand, these constrictions are wide enough to allow the passage of catalyst 1 (during immobilization), substrate 2 (during RCM), and MMC product 3. Oligomer formed outside these regions (indicated in yellow) can move freely through the remaining pore system.

in Figure 7 becomes particularly important when high substrate concentrations move into the focus due to the increasing significance of ADMET.

3. Conclusions

Presented Eqs. (2)–(7) quantify hindered accessibility and diffusion in realistic geometrical models of random mesoporous silicas intended for subsequent application as support in the RCM of substrate 2, with catalyst 1 selectively immobilized inside their mesopores. Using the individual values for ϵ_0 and τ_0 in Eqs. (6) and (7), i.e., $\epsilon_0 = 0.601$ and $\tau_0 = 1.69$ for Si60 ($d_{\text{meso}} = 5.9 \text{ nm}$) and $\epsilon_0 = 0.691$ and $\tau_0 = 1.41$ for Si100 ($d_{\text{meso}} = 13 \text{ nm}$), the two expressions quantify the hindrance to diffusion through

the respective silica material as experienced by finite-size, passive tracers for $\lambda = d_{\text{tracer}}/d_{\text{meso}}$ (ratio between tracer size and mean mesopore diameter) up to ~ 0.7 (Si60) and ~ 0.6 (Si100). Within these ranges, Eqs. (2)–(7) can be generally used to predict transport properties for the employed silica particles. Ideally, the relationships are known before a material is used as support in a specific application. The elaborate reconstruction-simulation approach underlying the establishment of this knowledge is justified considering that the highly detailed information provided can become a decisive factor to boost performance in a process that depends on efficient and/or selective transport of finite-size solutes.

The quantitative morphology-transport relationships have been adapted to discuss pore space accessibility and hindered diffusion with respect to the immobilization, formation, and

transport of key molecular species 1–4 in the RCM of the α,ω -vinylc pro lactone 2 to MMC product 3 and oligomer 4, with catalyst 1 selectively immobilized inside the mesopores of the silica particles. This analysis has shown that already the immobilization step requires careful consideration of size-exclusion effects (on the achievable loading of the particles with the catalyst) and diffusive hindrance factors (governing the timescale of uniform immobilization throughout the particles). The next important consideration was the substrate size. Substrate 2 is slightly smaller than the catalyst, so that it can access all catalytic centers inside the mesopores. If substrate molecules were larger than the catalyst during immobilization, a fraction of the catalytic centers would be unavailable for the metathesis pathways. Based on molecular size, direct macrocyclization of the substrate 2 to the MMC product 3 is favored over oligomerization to 4 in both studied silicas, as reflected by the differences in accessible porosities and diffusive hindrance factors for 3 and 4 (Table 2). This preference is more distinctive for Si60 than for Si100, which is recognized in the steeper slopes of the accessible porosity and hindered diffusivity curves for Si60 in the range of tracer sizes relevant to 3 and 4 (gray-shaded regions in Figure 4). However, improved size-selectivity is accompanied by reduced mobility and there appears to be a fine line between the antagonistic effects on selectivity and conversion induced by the confinement. As a particular feature of the confinement, we identified by direct image analysis pore regions in the silica that could trap (locally formed) oligomer due to size-selective passage resulting from constrictions. To what extent this trapped matter will be detected after an experiment depends on the timescale of the experiment and the dynamics of further reactions of the oligomer.

Importantly, the derived morphology-transport relationships can be applied to other catalysts, substrates, and products in straightforward manner to assess transport resistances and transport selectivities. For that purpose, the hydrodynamic diameters of key molecular species (required for λ in Eqs. (2)–(7)) can be estimated in the solvent of interest using DOSY-NMR. Together with complementary experimental data on conversion and selectivity, the deduced information will help to unravel complex reaction pathways and to better understand mechanistic aspects of olefin metathesis, as addressed in Figure 7. Furthermore, if also relevant reaction kinetic data are available, the morphology-based hindered diffusion coefficients will improve relationships between effectiveness factor and Thiele modulus and thereby the predictions on microreactor operation (diffusion vs. reaction control) and the proper selection of the particle size.

Currently, we use the silica particles in RCM experiments in a continuous-flow microreactor setup that allows to assign conversion and selectivity to well-defined reaction times and, thus, to analyze multiple reaction times and temperatures fully automated in a single flow experiment. The combined approach to morphology-transport-functionality relationships will pave the way to fast and systematic screenings of catalyst activity, conversion, and selectivity in dependence of spatial confinement effects, in particular, with a straightforward variation of the mesoporous support, type and loading of catalyst, type and

concentration of substrate, solvent, reaction time, and temperature. Results will be reported in due course.

Experimental Section

Material characterization: Nitrogen physisorption measurements were carried out at 77 K on a Thermo Scientific Surfer gas adsorption porosimeter (Thermo Fisher Scientific, Waltham, MA). Prior to the measurements, the samples were evacuated for 10 h at 250 °C. Total pore volumes (V_t) were obtained with the Gurvich rule at a relative pressure of $p/p_0 = 0.95$, specific surface areas (S_{BET}) were determined by means of the Brunauer-Emmett-Teller equation in the range of $0.05 \leq p/p_0 \leq 0.3$. Pore size distributions were derived from the adsorption branches of the physisorption isotherms using the non-local density functional theory (NLDFT) method with a cylindrical pore model.^[23]

Electron tomography: Scanning transmission electron microscopy (STEM) tomography was employed to obtain physical reconstructions of two silicas.^[12] For preparation, powder samples were ground in a mortar and subsequently dusted over a holey Cu grid (Quantifoil Micro Tools, Jena, Germany). Au fiducial markers were added to the sample crumbs from aqueous solution. Electron tomographic data were collected using an image-corrected Titan 80-300 transmission electron microscope (FEI, Hillsboro, OR) at an acceleration voltage of 300 kV. The microscope was operated in STEM mode with a nominal beam diameter of 0.2 nm. STEM tilt-series were recorded over a range of $\pm 76^\circ$ (Si60) and from -76° to 70° (Si100) in increments of 2° with a high-angle annular dark-field collector. Images were then aligned in IMOD 4.7 by means of the Au reference markers.^[24] The average alignment error was < 1 pixel. After applying a sufficient number of iterations (100 for Si60 and 25 for Si100) of the SIRT-algorithm to the aligned image series using the Xplore3D software package (version 3.0, FEI), the reconstructions were denoised by employing the ImageJ plugins Filters/Median 3D and Enhance Local Contrast (CLAHE).^[25,26] Final reconstructions were received after applying 10 iterations of DART using Fiji software and the ImageJ plugin TomoJ.^[27] For each sample, four cuboids were prepared as final reconstructions, covering different regions within the crumbs that were used for electron tomography. Image stacks had a voxel size of 0.23^3 nm^3 for Si60 and 0.32^3 nm^3 for Si100 (Figure S1, Supporting Information) and served as geometrical models for morphological analysis and the pore-scale simulations of hindered diffusion.

Diffusion simulations: A random-walk particle-tracking (RWPT) method was employed to simulate diffusive transport through the pore volumes of the eight reconstructions (cf. Figure S1).^[28] The method is based on the equivalence of the diffusion equation (where D denotes the diffusion coefficient and c concentration)

$$\frac{\partial c(\mathbf{r}, t)}{\partial t} = D \nabla^2 c(\mathbf{r}, t) \quad (8)$$

and the stochastic differential equation describing the random walk of a tracer, presented in discrete form as

$$\mathbf{r}(t + \delta t) = \mathbf{r}(t) + \Delta \mathbf{r} = \mathbf{r}(t) + \alpha \sqrt{6D\delta t} \quad (9)$$

In Eq. (9), $\mathbf{r}(t)$ denotes tracer position at time t , δt is the elementary time step of the random walk, and α is a vector with random orientation in space and a length governed by a Gaussian distribution with zero mean and unity variance. Initially, a large number of $N = 10^6$ passive (nonadsorbing, nonreacting) tracers was distributed randomly and uniformly in the entire void space of a

reconstruction. At the external faces of a reconstruction, the tracer displacement was handled by a mirror-boundary condition, which has been validated before and assumes that tracers crossing an external face of a reconstruction continue their motion in the mirror image of the original domain.^[14a] It enables complete sampling of the accessible pore space by the tracer ensemble at any time and therefore reflects spatially averaged morphological properties of a reconstruction along with their impact on diffusive transport. During each time step δt (small enough that the mean diffusive displacement did not exceed $\Delta h/10$, where Δh is the spatial resolution of a reconstruction), the displacement of every tracer by random diffusive motion was determined according to Eq. (9). A multiple-rejection boundary condition at the surface was used to model passive interaction of the tracers with the impermeable pore walls:^[29] when a tracer hit the impermeable wall during an iteration, the displacement was rejected and recalculated until tracer position was in the void space. The accuracy of the employed RWPT-approach including the described boundary conditions has been confirmed by comparing diffusion coefficients simulated in regular arrays of spheres^[30] with values determined by the analytical approach.^[31] After each time step, all tracer positions were monitored and used to calculate a time-dependent diffusion coefficient $D(t)$ from

$$D(t) = \frac{1}{6N} \frac{d}{dt} \sum_{i=1}^N [\Delta r_i(t)]^2 \quad (10)$$

where $\Delta r_i(t)$ represents the displacement of the i th tracer after time t . The targeted effective, i.e., time-independent diffusion coefficients $D_{\text{eff},K}$ (locally within the mesopore network of a reconstruction, subscript K) were determined from the asymptotes of the transient diffusion curves observed in the long-time limit, as illustrated in Figure S2 (Supporting Information).

In contrast to pointlike tracers, which can access the entire void space in a reconstruction, the void space accessible to finite-size tracers is smaller due to their steric interaction with the impermeable pore walls. Considering the case of diffusion in a cylindrical pore, the center of a hard spherical tracer particle of diameter d_{tracer} is excluded from an annular region of thickness $d_{\text{tracer}}/2$ at the wall, i.e., the void space accessible to the center of a finite-size tracer becomes identical to the void space accessible to a pointlike tracer if the pore diameter is reduced by d_{tracer} . An extension of this isomorphism concept to random porous media has been proposed.^[21] According to this approach, the reduction of accessible pore space for finite-size tracers can be accounted for by eroding pore space accessible to pointlike tracers with a structuring element of size d_{tracer} (as illustrated in Figure 3).^[14a,32] We implemented this mathematical morphology operation to generate accessible mesopore space in the eight reconstructions (cf. Figure S1) for d_{tracer} -values from 0 to 4.14 nm in 0.46-nm steps (Si60) and from 0 to 7.68 nm in 0.64-nm steps (Si100).

By adapting this approach for the RWPT-simulations, accessible porosity $\varepsilon(\lambda)$ and effective diffusion coefficient within a reconstruction $D_{\text{eff},K}(\lambda)$ were determined for different tracer sizes as a function of $\lambda = d_{\text{tracer}}/d_{\text{mesop}}$ the ratio between tracer size and mean mesopore diameter (cf. Figures 4 and 6). With the λ -dependent values of the local hindrance factor, $K_d(\lambda) = D_{\text{eff},K}(\lambda)/D_m$, the associated global hindrance factor $H(\lambda)$ could be derived (cf. Eqs. (6) and (7)) through the accessible porosity $\varepsilon(\lambda)$, determined as the void volume fraction of an eroded pore space at this λ . The program realization of the RWPT-algorithm was implemented as a parallel code in C language using the Message Passing Interface (MPI) standard on a supercomputing platform at the Philipps-Universität Marburg (Marburg, Germany).

Diffusion measurements: Diffusion coefficients in bulk solution (deuterated benzene for 1, deuterated toluene for 2–4) were determined via DOSY-NMR carried out at 298 K on a Bruker Avance III 400 spectrometer. For these measurements, homogeneous catalyst 1 and a mixture of substrate 2, MMC product 3, and oligomer 4 have been prepared as described previously.^[18] Hydrodynamic diameters d_h (cf. Table 2) were then calculated from these diffusion coefficients in bulk solution by application of the Stokes-Einstein equation.

Supporting Information

Supporting Information is available from the Wiley Online Library or from the author.

Acknowledgement

We gratefully acknowledge financial support by the Deutsche Forschungsgemeinschaft (DFG, Bonn, Germany, grant number 358283783 – CRC 1333). This work was also supported by the Karlsruhe Nano Micro Facility (KNMF) at the Karlsruhe Institute of Technology (Karlsruhe, Germany) under the KNMF long-term user proposal 2020-024-029294. We further thank Richard Kohns and Professor Dirk Enke (Institute of Chemical Technology, Universität Leipzig, Leipzig, Germany) for the nitrogen physisorption measurements and Benjamin Peters (Instrumental Analytics R&D, Merck KGaA, Darmstadt, Germany) for the generous gift of the silica particles. Open access funding enabled and organized by Projekt DEAL.

Conflict of Interest

The authors declare no conflict of interest.

Keywords: electron tomography · heterogeneous catalysis · hindered diffusion · mesoporous materials · metathesis

- [1] a) R. Anwander, *Handbook of Heterogeneous Catalysis* (Eds.: G. Ertl, H. Knözinger, F. Schüth, J. Weitkamp), VCH-Weinheim 2008, Volume 1, pp. 583–613; b) Y. Liu, H. Tsunoyama, T. Akita, T. Tsukuda, *J. Phys. Chem. Lett.* 2009, 113, 13457–13461; c) L.-B. Sun, J.-R. Li, W. Lu, Z.-Y. Gu, Z. Luo, H.-C. Zhou, *J. Am. Chem. Soc.* 2012, 134, 15923–15928; d) D. I. Fried, F. J. Brieler, M. Fröba, *ChemCatChem* 2013, 5, 862–884; e) Z. Zhou, M. Hartmann, *Chem. Soc. Rev.* 2013, 42, 3894–3912; f) G. Cottone, S. Giurida, S. Bettati, S. Bruno, B. Campanini, M. Marchetti, S. Abbruzzetti, C. Viappiani, A. Cupane, A. Mozzarelli, L. Ronda, *Catalysts* 2019, 9, 1024; g) R. Kohns, N. Anders, D. Enke, U. Tallarek, *Adv. Mater. Interfaces* 2020, DOI: 10.1002/admi.202000163.
- [2] a) C. N. Satterfield, *Mass Transfer in Heterogeneous Catalysis*, MIT Press, Cambridge, MA 1970; b) C. N. Satterfield, C. K. Colton, W. H. Pitcher, *AIChE J.* 1973, 19, 628–635; c) S.-J. Reich, A. Svidrytski, A. Hölzel, J. Florek, F. Kleitz, W. Wang, C. Kübel, D. Hlushkou, U. Tallarek, *J. Phys. Chem. C* 2018, 122, 12350–12361.
- [3] a) T. Kjellman, X. Xia, V. Alfredsson, A. E. Garcia-Bennett, *J. Mater. Chem. B* 2014, 2, 5265–5271; b) J. H. Lee, Y. Yeo, *Chem. Eng. Sci.* 2015, 125, 75–84; c) R.-A. Mitran, C. Matei, D. Berger, *J. Phys. Chem. C* 2016, 120, 29202–29209; d) R. Diab, N. Canilho, I. A. Pavel, F. B. Haffner, M. Girardon, A. Pasc, *Adv. Colloid Interface Sci.* 2017, 249, 346–362.

- [4] H. S. Fogler, *Elements of Chemical Reaction Engineering*, 4th Ed., Prentice Hall, Upper Saddle River, NJ 2006.
- [5] a) F. Goettmann, C. M. Sanchez, *J. Mater. Chem.* **2007**, *17*, 24–30; b) C. Yu, J. He, *Chem. Commun.* **2012**, *48*, 4933–4940; c) V. Mouarrawis, R. Plessius R, J. I. van der Vlugt, J. N. H. Reek, *Front. Chem.* **2018**, *6*, 623; d) Z. Zhao, *ChemCatChem* **2020**, *12*, 1–23.
- [6] a) W. M. Deen, *AIChE J.* **1987**, *33*, 1409–1425; b) P. Dechadilok, W. M. Deen, *Ind. Eng. Chem. Res.* **2006**, *45*, 6953–6959.
- [7] a) J. Kärger, D. M. Ruthven, D. N. Theodorou, *Diffusion in Nanoporous Materials*, Wiley-VCH, Weinheim **2012**; b) I. L. C. Buurmans, B. M. Weckhuysen, *Nat. Chem.* **2012**, *4*, 873–886.
- [8] a) C. Chmelik, J. Kärger, *Chem. Soc. Rev.* **2010**, *39*, 4864–4884; b) C. D'Agostino, J. Mitchell, L. F. Gladden, M. D. Mantle, *J. Phys. Chem. C* **2012**, *116*, 8975–8982; c) M. Goepel, H. Kabir, C. Küster, E. Saraçi, P. Zeigermann, R. Valiullin, C. Chmelik, D. Enke, J. Kärger, R. Gläser, *Catal. Sci. Technol.* **2015**, *5*, 3137–3146; d) A. Galarneau, F. Guenneau, A. Gedeon, D. Mereib, M. Rodriguez, F. Fajula, B. Coasne, *J. Phys. Chem. C* **2016**, *120*, 1562–1569; e) F. Elwinger, P. Pourmand, I. Furó, *J. Phys. Chem. C* **2017**, *121*, 13757–13764; f) T. J. Rottreau, C. M. A. Parlett, A. F. Lee, R. Evans, *J. Phys. Chem. C* **2017**, *121*, 16250–16256; g) C. D'Agostino, M. D. Mantle, L. F. Gladden, *Microporous Mesoporous Mater.* **2018**, *269*, 88–92; h) S. Kolitcheff, E. Jolimitre, A. Hugon, J. Verstraete, M. Rivallan, P.-L. Carrette, F. Couennea, M. Tayakout-Fayolle, *Catal. Sci. Technol.* **2018**, *8*, 4537–4549; i) J. Kärger, D. Freude, J. Haase, *Process* **2018**, *6*, 147; j) M. A. Isaacs, N. Robinson, B. Barbero, L. J. Durrndell, J. C. Manayil, C. M. A. Parlett, C. D'Agostino, K. Wilson, A. F. Lee, *J. Mater. Chem. A* **2019**, *7*, 11814–11825; k) L. Forster, M. Lutecki, H. Fordsmand, L. Yu, C. D'Agostino, *Mol. Syst. Des. Eng.* **2020**, *5*, 1193–1204.
- [9] a) J. Michaelis, C. Bräuchle, *Chem. Soc. Rev.* **2010**, *39*, 4731–4740; b) D. A. Higgins, S. C. Park, K.-H. Tran-Ba, T. Ito, *Annu. Rev. Anal. Chem.* **2015**, *8*, 193–216; c) L. D. C. Bishop, C. F. Landes, *Acc. Chem. Res.* **2018**, *51*, 2247–2254.
- [10] L. Kisley, R. Brunetti, L. J. Tazuin, B. Shuang, X. Y. Yi, A. W. Kirkeminde, D. A. Higgins, S. Weiss, C. F. Landes, *ACS Nano* **2015**, *9*, 9158–9166.
- [11] T. Titze, C. Chmelik, J. Kullmann, L. Prager, E. Miersemann, R. Gläser, D. Enke, J. Weitkamp, J. Kärger, *Angew. Chem. Int. Ed.* **2015**, *54*, 5060–5064; *Angew. Chem.* **2015**, *127*, 5148–5153.
- [12] a) C. Kübel, A. Voigt, R. Schoenmakers, M. Otten, D. Su, T.-C. Lee, A. Carlsson, J. Bradley, *Microsc. Microanal.* **2005**, *11*, 378–400; b) H. Friedrich, P. E. de Jongh, A. J. Verkleij, K. P. de Jongh, *Chem. Rev.* **2009**, *109*, 1613–1629; c) R. Leary, P. A. Midgley, J. M. Thomas, *Acc. Chem. Res.* **2012**, *45*, 1782–1791; d) A. B. Hungria, J. J. Calvino, J. C. Hernández-Garrido, *Top. Catal.* **2019**, *62*, 808–821.
- [13] a) F. Tariq, P. D. Lee, R. Haswell, D. W. McComb, *Chem. Eng. Sci.* **2011**, *66*, 5804–5812; b) S. Mitchell, N.-L. Michels, K. Kunze, J. Pérez-Ramírez, *Nat. Mater.* **2012**, *4*, 825–831; c) J.-D. Grunwaldt, J. B. Wagner, R. E. Dunin-Borkowski, *ChemCatChem* **2013**, *5*, 62–80; d) S. Mitchell, A. B. Pinar, J. Kevin, P. Crivelli, J. Kärger, J. Pérez-Ramírez, *Nat. Commun.* **2015**, *6*, 8633; e) U. Tallarek, D. Hlushkou, J. Rybka, A. Höltzel, *J. Phys. Chem. C* **2019**, *123*, 15099–15112; f) J. Becher, T. L. Sheppard, Y. Fam, S. Baier, W. Wang, D. Wang, S. Kulkarni, T. F. Keller, M. Lyubomirskiy, D. Brueckner, M. Kahnt, A. Schropp, C. G. Schroer, J.-D. Grunwaldt, *J. Phys. Chem. C* **2019**, *123*, 25197–25208; g) J. Jankovic, S. Zhang, A. Putz, M. S. Saha, D. Susac, *J. Mater. Res.* **2019**, *34*, 579–591; h) F. Gritti, J. Hochstrasser, A. Svidrytski, D. Hlushkou, U. Tallarek, *J. Chromatogr. A* **2020**, *1620*, 460991.
- [14] a) D. Hlushkou, A. Svidrytski, U. Tallarek, *J. Phys. Chem. C* **2017**, *121*, 8416–8426; b) S.-J. Reich, A. Svidrytski, D. Hlushkou, D. Stoeckel, C. Kübel, A. Höltzel, U. Tallarek, *Ind. Eng. Chem. Res.* **2018**, *57*, 3031–3042; c) S.-J. Reich, A. Svidrytski, A. Höltzel, W. Wang, C. Kübel, D. Hlushkou, U. Tallarek, *Microporous Mesoporous Mater.* **2019**, *282*, 188–196; d) J. Hochstrasser, A. Svidrytski, A. Höltzel, T. Priamushko, F. Kleitz, W. Wang, C. Kübel, U. Tallarek, *Phys. Chem. Chem. Phys.* **2020**, *22*, 11314–11326.
- [15] E. M. Renkin, *J. Gen. Physiol.* **1954**, *38*, 225–243.
- [16] a) C. Copéret, J. M. Basset, *Adv. Synth. Catal.* **2007**, *349*, 78–92; b) M. R. Buchmeiser, *Chem. Rev.* **2009**, *109*, 303–321; c) H. Balcar, J. Čejka, *Coord. Chem. Rev.* **2013**, *257*, 3107–3124; d) M. R. Buchmeiser, *Olefin Metathesis: Theory and Praxis* (Ed.: K. Grela), John Wiley & Sons, Hoboken, NJ **2014**, pp. 495–514; e) A. Dewaele, F. Verpoort, B. Sels, *ChemCatChem* **2016**, *8*, 3010–3030; f) R. Zhong, A. C. Lindhorst, F. J. Groche, F. E. Kühn, *Chem. Rev.* **2017**, *117*, 1970–2058; g) W. Wang, L. Cui, P. Sun, L. Shi, C. Yue, F. Li, *Chem. Rev.* **2018**, *118*, 9843–9929; h) C. Copéret, F. Allouche, K. W. Chan, M. P. Conley, M. F. Delley, A. Fedorov, I. B. Moroz, V. Mougél, M. Pucino, K. Searles, K. Yamamoto, P. A. Zhizhko, *Angew. Chem. Int. Ed.* **2018**, *57*, 6398–6440; *Angew. Chem.* **2018**, *130*, 6506–6551.
- [17] a) S. Derouane, *J. Catal.* **1986**, *100*, 541–544; b) Special issue on confinement effects: *J. Mol. Catal. A: Chem.* **2009**, *305*, 1–190.
- [18] F. Ziegler, J. Teske, I. Elser, M. Dyballa, W. Frey, H. Kraus, N. Hansen, J. Rybka, U. Tallarek, M. R. Buchmeiser, *J. Am. Chem. Soc.* **2019**, *141*, 19014–19022.
- [19] M. Thommes, K. Kaneko, A. V. Neimark, J. P. Olivier, F. Rodriguez-Reinoso, J. Rouquerol, K. S. W. Sing, *Pure Appl. Chem.* **2015**, *87*, 1051–1069.
- [20] I. Bacsckay, A. Sepsey, A. Felinger, *J. Chromatogr. A* **2014**, *1339*, 110–117.
- [21] a) S. Torquato, *J. Chem. Phys.* **1991**, *95*, 2838–2841; b) I. C. Kim, S. Torquato, *J. Chem. Phys.* **1992**, *96*, 1498–1503.
- [22] S. Monfette, D. E. Fogg, *Chem. Rev.* **2009**, *109*, 3783–3816.
- [23] K. A. Cychosz, R. Guillet-Nicolas, J. Garcia-Martinez, M. Thommes, *Chem. Soc. Rev.* **2017**, *46*, 389–414.
- [24] J. R. Kremer, D. N. Mastronarde, J. R. McIntosh, *J. Struct. Biol.* **1996**, *116*, 71–76.
- [25] P. Gilbert, *J. Theor. Biol.* **1972**, *36*, 105–117.
- [26] J. Schindelin, I. Arganda-Carreras, E. Frise, V. Kaynig, M. Longair, T. Pietzsch, S. Preibisch, C. Rueden, S. Saalfeld, B. Schmid, J.-Y. Tinevez, D. J. White, V. Hartenstein, K. Eliceiri, P. Tomancak, A. Cardona, *Nat. Methods* **2012**, *9*, 676–682.
- [27] C. Messaoudil, T. Boudier, C. O. S. Sorzano, S. Marco, *BMC Bioinf.* **2007**, *8*, 288.
- [28] J. Salles, J.-F. Thovert, L. Delannay, L. Prevors, J.-L. Aurialt, P. M. Adler, *Phys. Fluids A* **1993**, *5*, 2348–2376.
- [29] P. Szymczak, A. J. C. Ladd, *Phys. Rev. E* **2003**, *68*, 036704.
- [30] a) H. Liasneuski, D. Hlushkou, S. Khirevich, A. Höltzel, U. Tallarek, S. Torquato, *J. Appl. Phys.* **2014**, *116*, 034904; b) A. Daneyko, D. Hlushkou, V. Baranau, S. Khirevich, S. Seidel-Morgenstern, U. Tallarek, *J. Chromatogr. A* **2015**, *1407*, 139–156.
- [31] M. H. Blees, J. C. Leyte, *J. Colloid Interface Sci.* **1994**, *166*, 118–127.
- [32] H. Koku, R. S. Maier, M. R. Schure, A. M. Lenhoff, *J. Chromatogr. A* **2012**, *1237*, 55–63.

Manuscript received: September 15, 2020

Revised manuscript received: September 30, 2020

Accepted manuscript online: October 2, 2020

Version of record online: November 2, 2020